


## RESEARCH ARTICLE

# Liq interlayer as electron extraction layer for highly efficient and stable perovskite solar cells

Kunsik An<sup>1</sup>  | Jaehoon Kim<sup>2</sup>  | Beomhee Yoon<sup>3</sup> | Hyunho Lee<sup>3</sup> 

<sup>1</sup>Department of Mechatronics Engineering, Konkuk University, Chungju, Republic of Korea

<sup>2</sup>Department of Electrical and Computer Engineering, Inter-University Semiconductor Research Center, Seoul National University, Seoul, Republic of Korea

<sup>3</sup>Department of Electronic Engineering, Kwangwoon University, Seoul, Republic of Korea

## Correspondence

Hyunho Lee, Department of Electronic Engineering, Kwangwoon University, 20 Kwangwoon-ro, Nowon-gu, Seoul 01897, Republic of Korea.  
Email: hyunho@kw.ac.kr

## Funding information

Kwangwoon University; National Research Foundation, Grant/Award Numbers: 2018R1A6A1A03025242, 2020R1F1A1074263

## Summary

Halide perovskite solar cells (PSCs) have gained enormous attention due to their favorable features such as bandgap tunability, considerable free carrier diffusion length, low-cost fabrication, and comparable efficiency to that of conventional silicon solar cells. Among several PSCs' structures, the inverted structure is the most suitable candidate for diverse portable applications since they can take advantage of the previously developed organic solar cells' structure. However, the single transporting layer system of the inverted-structured PSCs makes it challenging to achieve high efficiency and operational stability. Here, we introduce a unique transporting layer system that adopts 8-hydroxyquinolinolato-lithium (Liq) as a buffer layer at the interface between [6,6]-phenyl C71 butyric acid methyl ester (PC<sub>70</sub>BM) and Ag electrode. By introducing the Liq, we effectively decreased the potential energy barrier and iodide accumulation at the interface between PC<sub>70</sub>BM and Ag electrode, which resulted in an efficient and stable PSC. In the optimized structure, the power conversion efficiency and stability (T<sub>80</sub>) increased from 9.5% and 100 h to 10.13% and 200 h, respectively.

## KEYWORDS

C-AFM, halide perovskite, inter layer, Liq, SKPM, TOF-SIMS

## 1 | INTRODUCTION

Halide perovskite has been investigated as a core source due to its superior optoelectronic characteristics in the visible wavelength range.<sup>1,2</sup> Halide perovskite can easily tune the absorption and emission wavelength range by merely controlling the bandgap with halide composition variation.<sup>3,4</sup> Furthermore, perovskite's significant charge carrier diffusion length makes it possible to adopt a sufficiently thick photoactive layer, making it easy to utilize the full range of visible wavelength range with a large absorption coefficient.<sup>5</sup> For the past decade, perovskite solar cells (PSCs) have exhibited rapid growth, and the

National Renewable Energy Laboratory-certified power conversion efficiency (PCE) exceeded 25%,<sup>6</sup> comparable to that of silicon solar cells that possess the most of the solar cell market. Besides, the PSC's solution-processability makes the halide perovskite a strong candidate for a next-generation application that enables foldable or portable devices.<sup>7-9</sup> Furthermore, inverted-structured PSCs can adopt the conventional organic solar cell structure,<sup>10-12</sup> making it more suitable for the portable energy source based on its flexibility. In specific, the inverted structure consists of a *p*-type hole transporting layer (HTL) above the transparent electrode and an *n*-type electron transport layer (ETL) beneath the reflective electrode, where the perovskite active layer is sandwiched between the HTL and ETL. For efficient

Kunsik An and Jaehoon Kim contributed equally to this study.

extraction of the free carriers from the photoactive layer, choosing the appropriate adjacent buffer layer is critical. For HTLs, various materials such as poly(3,4-ethylenedioxythiophene) polystyrene sulfonate (PEDOT:PSS),<sup>10,13,14</sup> poly(triaryl amine) (PTAA),<sup>11,15</sup> and NiO<sup>16-18</sup> have been widely adopted. On the other hand, for the ETLs, diverse candidates such as [6,6]-phenyl C71 butyric acid methyl ester (PC<sub>70</sub>BM),<sup>10</sup> C<sub>60</sub>,<sup>19-22</sup> and ZnO<sup>20,22,23</sup> have been adopted since these candidates offer appropriate energy level alignment with reduced charge injection barrier for PSCs.

Among several recent technical issues in the charge transporting layers, the iodide ion migration from the active layer to the ETL/cathode is crucial for the PSCs' operational stability.<sup>24,25</sup> An additional buffer layer such as bathocuproine (BCP) has been introduced to address these problems,<sup>26</sup> but a severe degradation issue remained. In addition, although some articles utilized metal oxides, including ZnO or TiO<sub>2</sub>, these materials increased the burden of unfavorable electronic trap states and additional process steps.<sup>27,28</sup> Therefore, it is essential to find a superb interfacial layer to effectively suppress the iodide ion migration and reduce the ion accumulation at the ETL/cathode interface, which is vital for efficient and stable PSCs.

Lithium Schiff-base cluster complexes such as 8-hydroxyquinolinolato-lithium (LiQ) or lithium fluoride (LiF) are considered a proper candidate for buffer layer between the active layer and the counter electrode. These materials are proven to accelerate electron transport and reduce the energy barrier at the interface. Babei et al reported that LiQ has good electron extraction property in PSCs.<sup>29</sup> Approximately 25% increase of efficiency was achieved with a combination of BCP and LiQ. However, the operational mechanism of the LiQ layer is ambiguous and still in the debate. An in-depth analysis of the effect of the LiQ layer's morphology on the PSCs' performance is needed because the morphology of LiQ is dramatically affected by varying thicknesses.

In this work, we modified the interfacial layer between the PC<sub>70</sub>BM and the Ag electrode to enhance charge extraction and suppress the iodide ion migration. By incorporating the LiQ layer into the interfacial layer, we have reduced the energy barrier between the PC<sub>70</sub>BM and Ag electrodes. The surface characterization method, conductive AFM (C-AFM), was used to compare the electronic properties of LiQ film with different thicknesses. With these measurements, the film growth mode of LiQ on the PC<sub>70</sub>BM/perovskite layer was verified. The charge transfer was optimized at the thickness of which the superlattice of LiQ was formed. LiQ-induced Ag electrode exhibits potential increment with 0.2 eV, making efficient ohmic contact between ETL and Ag electrode. The transient dynamics also confirmed efficient charge transfer

characteristics with optimized LiQ thickness. Most importantly, we found that the insertion of the LiQ showed enhanced device lifetime mainly attributed to the improved stability of short-circuit current ( $J_{SC}$ ) and FF. For systematic analysis of ion migration, we conducted a time-of-flight secondary ion mass spectrometry (TOF-SIMS) on the devices with various conditions, which revealed the iodide accumulation-lowering effect by the insertion of LiQ layer. We finally suggest that our interfacial layer effectively suppressed the ion migration from the perovskite layer to the Ag electrode, which resulted in efficient and stable perovskite solar cells.

## 2 | EXPERIMENTAL SECTION

LiQ was purchased from Sigma-Aldrich as a powder form. PEDOT:PSS (AI4083) was purchased from Heraeus. Methylammonium iodide (MAI, 99.5%) was purchased from Xian Polymer Light Technology. Lead iodide (PbI<sub>2</sub>, 99.9985%) was purchased from Alfa Aesar. PC<sub>70</sub>BM was purchased from 1-Material. Dimethylformamide (DMF), dimethyl sulfoxide (DMSO), isopropyl alcohol (IPA), and chlorobenzene (CB) were purchased from Sigma-Aldrich. All materials were used as received without any purification.

The device fabrication procedures are as follows. Indium tin oxide (ITO) patterned glass substrates were sequentially cleaned by acetone, isopropyl alcohol, and deionized water. Dried substrates were treated with UV-ozone for 20 min. PEDOT:PSS, AI4083, Heraeus) were filtered (PTFE, 0.45  $\mu$ m) and spin-coated (3500 rpm, 30 s). PEDOT:PSS coated substrates were transferred to the hotplate and annealed (120°C, 20 min). After cooling down to room temperature, substrates were moved to an Ar-filled glovebox to deposit the perovskite layer. Perovskite film was formed by the two-step inter-diffusion method. PbI<sub>2</sub> (lead iodide, 99.999%, Alfa Aesar) was dissolved in DMF (Sigma-Aldrich)/DMSO (Sigma Aldrich) mixed solvent. MAI (Xian polymer) was dissolved in IPA. Specifically, 553 mg of PbI<sub>2</sub> (1.2 M) was dissolved in the mixture of 0.9 mL of DMF and 0.1 mL of DMSO. 100 mg of MAI was dissolved in 2 mL of IPA. The PbI<sub>2</sub> solution was stirred overnight under 70°C. 35  $\mu$ L of PbI<sub>2</sub> solution was dispersed on PEDOT:PSS coated substrate and spin-coated (3000 rpm, 30 s) without post-annealing. After 2 min, the MAI solution was quickly dispersed on transparent PbI<sub>2</sub> film and spin-coated (3000 rpm, 30 s). The brownish transparent pre-perovskite film was transferred to a 100°C hotplate (2 h) immediately. After cooling down to room temperature, PC<sub>70</sub>BM ([6,6]-phenyl C71 butyric acid methyl ester, Nano clean tech.) solution (23 mg/mL in chlorobenzene) was spin-coated (2000 rpm, 30 s). In brief, PC<sub>70</sub>BM is chosen for the ETL

rather than PC<sub>60</sub>BM due to better diode characteristics without non-ideal features such as S-shape (Figure S1). The PC<sub>70</sub>BM coated substrates were kept in a dry box (humidity under 20%) overnight. Then, the thickness controlled Liq layer and 100 nm of Ag electrode was thermally evaporated under  $\sim 10^{-6}$  Torr.

The photovoltaic parameters were measured using a 300 W solar simulator (Newport 91160A) under AM 1.5G ( $100 \text{ mW/cm}^2$ ) illumination. The effective device area was  $0.02 \text{ cm}^2$ , which is in a similar range to the former articles' active area size.<sup>30,31</sup> Cross-sectional and surface field emission scanning electron microscope images were taken by AURIGA (Carl Zeiss). X-ray diffraction (XRD) was measured by D8-advance (Bruker Miller). Time-resolved photoluminescence was measured using HALCYONE femtosecond fluorescence spectrometer (Ultrafast Systems). The sample was excited using a second harmonic Ti:sapphire laser (Mai-Tai, Spectra Physics), providing hundreds of 400 nm (3.1 eV) femtosecond pulse with a repetition rate of 8 MHz. Decay profiles were obtained by conventional time-correlated single-photon counting technique, using MPD-PDM Series DET-40 photon-counting detector and Pendulum CNT-91 frequency counter combined with a monochromator fixed at sample PL maxima. TOF-SIMS were measured using a secondary ion mass

spectrometer (ION-TOF). Cesium (Cs) was used as a sputter source with 1 keV energy and 50 nA current. The sputtering area was  $150 \times 150 \mu\text{m}^2$ . C-AFM was measured using a commercial atomic force microscope (XE-100, Park Systems Corp.). The local current was collected with a platinum-coated contact-mode tip cantilever (Nanosensors) under 0.7 V bias onto the sample side. Scanning Kelvin probe microscopy (SKPM) is also conducted with the same microscope equipment. The image was taken by applying AC voltage of 2 V amplitude and 17 kHz frequency with Cr/Au coated noncontact-mode tip cantilever (Nanosensors). All of the measurements were performed in ambient air at room temperature.

### 3 | RESULTS AND DISCUSSION

#### 3.1 | Device performance of PSCs with Liq interfacial layer

PSCs were fabricated regarding the following structure to examine the interfacial layer effect of Liq. Schematic illustration and energy band diagram of PSC with the inverted structure of ITO/PEDOT:PSS/CH<sub>3</sub>NH<sub>3</sub>PbI<sub>3</sub>/PC<sub>70</sub>BM/Liq/Ag are shown in Figure 1A and Figure S2.

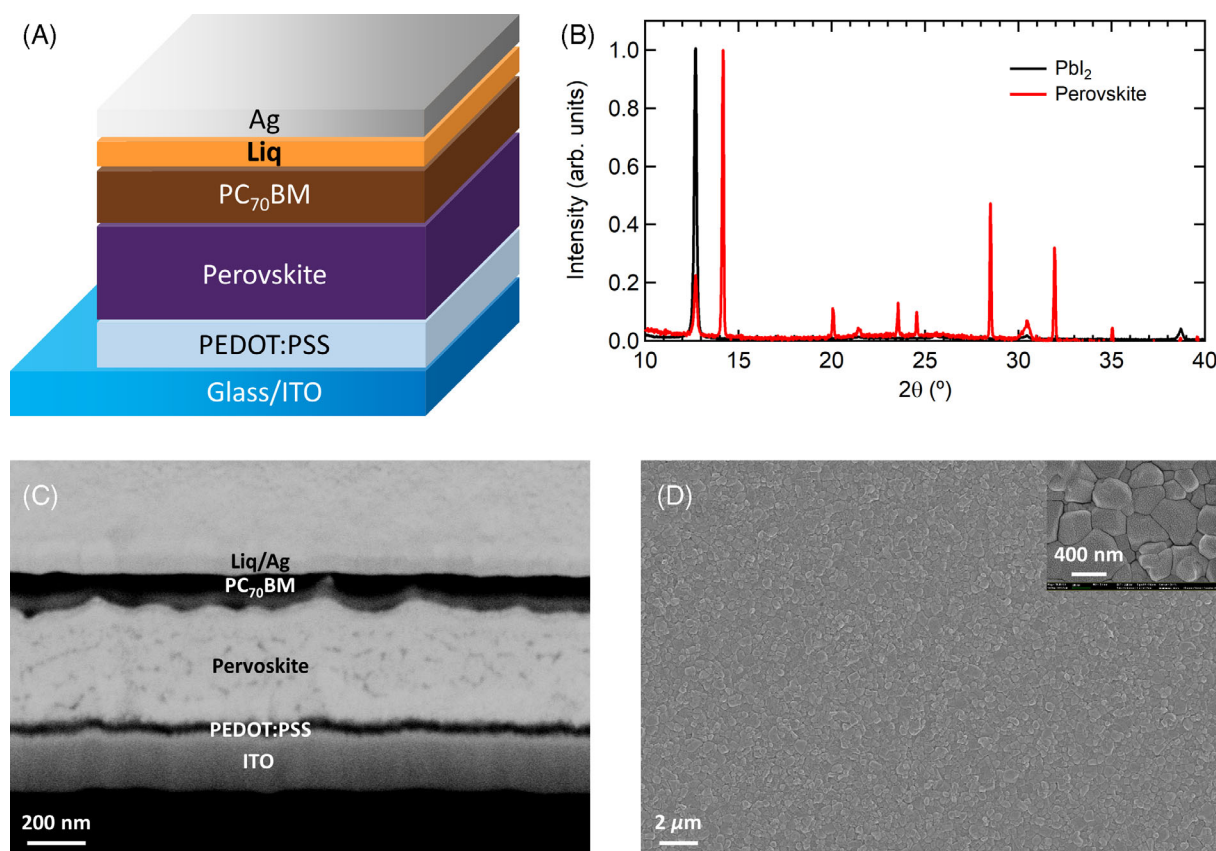


**FIGURE 1** A, Device architecture of PSC; B, XRD of PbI<sub>2</sub> and perovskite film with a 2-step fabrication process; C, cross view; D, top view of PSC by SEM

While the  $\text{PbI}_2$  film showed a representative crystallinity peak of  $12.5^\circ$ , the perovskite film, fabricated through the 2-step process, showed strong perovskite crystalline peaks around  $14^\circ$ ,  $28.5^\circ$ , and  $32^\circ$  (110, 220, and 310 planes, respectively) (Figure 1B), where highly crystalline perovskite film is essential for efficient device performance.<sup>32–34</sup>

Uniform and compact perovskite film formation are essential for obtaining efficient charge transport properties and reliable device performance.<sup>35,36</sup> However, achieving a compact perovskite film is often challenging, which easily results in inferior electrical characteristics and device performance. Nonetheless, device architecture with compact and uniform films was fabricated through a 2-step process (Figure 1C,D). In specific, the cross-section of the device merely showed pinholes (Figure 1C). Similarly, the film's surface also showed compact morphology with an average grain size of 300 nm, which is in line with the articles reporting the grain size of 350 nm for efficient perovskite film (Figure 1D).<sup>37</sup>

The  $J$ - $V$  characteristics and respective photovoltaic parameters are plotted as a function of Liq thickness (Figure 2). The  $J$ - $V$  characteristics showed identical behavior upon various measurement conditions of measurement delay time (Figure S3), scan direction (Figure S4) and offered reliable  $J_{\text{SC}}$  and PCE upon intermittent and continuous light illumination (Figure S5 and S6). The PSCs' photovoltaic characteristics increased to the maximum as Liq thickness increased to 5 nm, while it inversely started to decrease at over 7 nm (Table 1). In brief, as the Liq thickness increased from 0 to 5 nm, the average photovoltaic parameters increased from  $J_{\text{SC}}$  (14.0  $\text{mA}/\text{cm}^2$ ),  $V_{\text{OC}}$  (0.88 V), FF (69.0%), PCE (8.48%) to  $J_{\text{SC}}$  (14.5  $\text{mA}/\text{cm}^2$ ),  $V_{\text{OC}}$  (0.88 V), FF (71.3%), and PCE (9.07%). Agreeing with the enhanced  $J_{\text{SC}}$ , the device with a 5 nm thick Liq layer showed a significant increase in incident-photon-to-current-efficiency (Figure S7). In the aspect of light intensity ( $P_{\text{light}}$ )-dependent  $J_{\text{SC}}$  and  $V_{\text{OC}}$ , the enhancement of device performance seemed to be relevant to the reduction of space-charge effect, charge imbalance, bimolecular recombination, or trap-assisted recombination (Figure S8).<sup>38</sup> However, contrary to the  $V_{\text{OC}}$ , the  $J_{\text{SC}}$  and FF showed a relevant change depending on the Liq thickness, which is in line with the PCE's trend. Since the  $J_{\text{SC}}$  and FF are sensitively affected by the charge extraction properties,<sup>39,40</sup> precise analyses should be conducted on the charge extraction. Although Liq's charge extraction elevation effect is widely proven in the organic light-emitting diodes<sup>41</sup> and organic photovoltaics,<sup>42</sup> it is rarely reported in PSCs. Thus, to validate the origin of the advantageous effect of the Liq

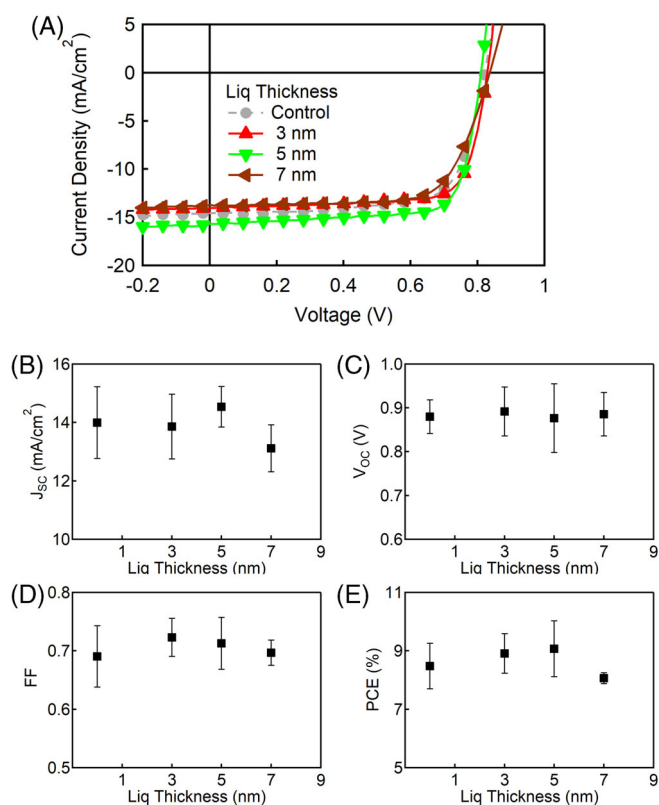


**FIGURE 2** A, Current-voltage ( $J$ - $V$ ) characteristics; B-E, photovoltaic parameters regarding the Liq thickness of (0, 3, 5, 7 nm)

layer, we conducted systematic and comprehensive analyses, including the C-AFM and SKPM, which offered clues for the phenomena.

### 3.2 | Morphological and optoelectronic characteristics of Liq films on $\text{PC}_{70}\text{BM}$

The uniform deposition of the Liq layer onto the  $\text{PC}_{70}\text{BM}$  surface was challenging because the target thickness of the Liq layer was below 10 nm. Furthermore, the severe lattice mismatch between Liq and  $\text{PC}_{70}\text{BM}$  causes non-uniform film growth during the deposition. The lattice parameters of Liq and  $\text{PC}_{70}\text{BM}$  are shown in Table S1.<sup>43,44</sup> The morphology of interfaces between the layers is determined by the interfacial misfit ( $\Delta\sigma$ ) and surface energy difference ( $\Delta a$ ). The interfacial misfit is defined as Equation (1), where  $\sigma_s$  and  $\sigma_o$  are surface energy of underlayer and overlayer, respectively. The surface energy difference is defined as Equation (2), where  $a_s$  and  $a_o$  are lattice parameters of underlayer and overlayer.

**TABLE 1** Current-voltage (*J-V*) characteristics<sup>a,b</sup> of PSCs with various Liq thickness

	Liq 0 nm	Liq 3 nm	Liq 5 nm	Liq 7 nm
$J_{SC}$ (mA cm <sup>-2</sup> )	14.0 ± 1.2	13.9 ± 1.1	14.5 ± 0.7	13.1 ± 0.8
$V_{OC}$ (V)	0.88 ± 0.04	0.89 ± 0.06	0.88 ± 0.08	0.89 ± 0.05
FF	69.0 ± 5.2	72.3 ± 3.3	71.3 ± 4.5	69.7 ± 2.2
PCE (%)	8.48 ± 0.78 (9.5)	8.91 ± 0.68 (9.8)	9.07 ± 0.96 (10.13)	8.06 ± 0.18 (8.28)

<sup>a</sup>Extracted based on 9 independent devices.<sup>b</sup>Values in the parentheses correspond to the highest data.

$$\Delta\sigma = \frac{\sigma_s - \sigma_o}{\sigma_s} \quad (1)$$

$$\Delta a = \frac{a_s - a_o}{a_s} \quad (2)$$

Based on the equations, the film formation of the overlayer is determined within three types.<sup>45,46</sup> Frank-van der Merwe mode occurs when the lattice mismatch is nearly zero, and the surface energy of the overlayer is less than that of the underlayer. The overlayer is grown epitaxially with the layer-by-layer structure at this mode. On the other hand, Weber-Volmer mode occurs when the lattice mismatch is high, and the surface energy difference is small. The overlayer deposits nonuniformly as an island-like morphology in this mode. Finally, Stranski-Krastanov mode combines both Frank-van der Merwe and Weber-Volmer modes, where an island grows after very thin superlattice layer formation. This mode occurs when the surface energy of the overlayer is higher than that of the underlayer with a large interfacial misfit, following Equations (3) and (4).

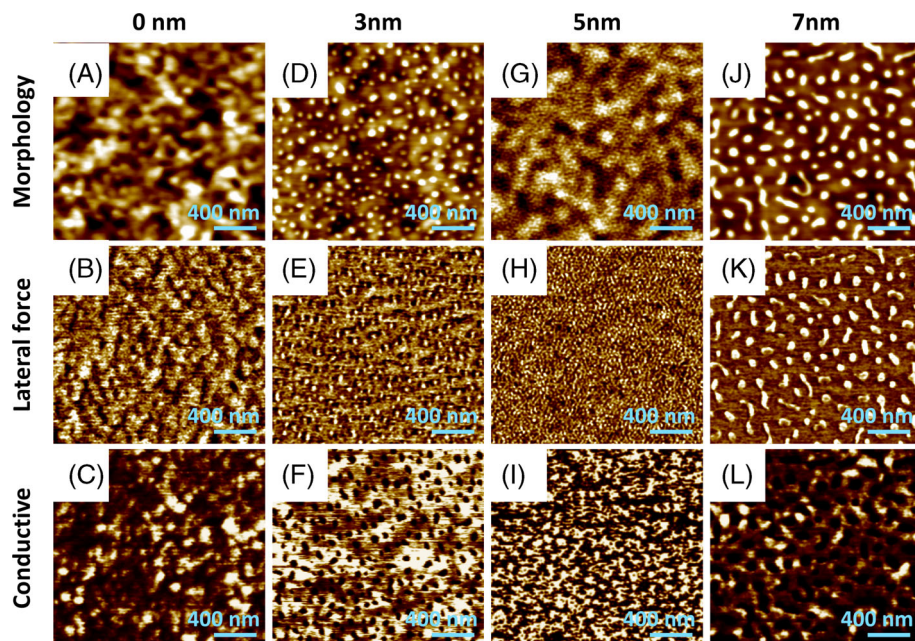
$$V = abc\sqrt{1 - \cos^2 \alpha - \cos^2 \beta - \cos^2 \gamma + 2\cos \alpha \cos \beta \cos \gamma} \quad (3)$$

$$W_{ls} = \sigma_1(1 + \cos \theta) \quad (4)$$

The Liq overlayer on the perovskite/PC<sub>70</sub>BM bilayer has too high interfacial mismatch to exhibit Frank-van der Merwe mode that the lattice parameters of Liq and PC<sub>70</sub>BM as shown in Table S1. For instances, lattice parameters of PC<sub>70</sub>BM in <100>, <010>, and <001> direction is 12.88, 15.1, and 18.18 nm respectively. The lattice parameters of Liq in <100>, <010>, and <001> direction is 9.24, 10.41, and 10.35 nm respectively. These values are calculated by dividing unit volume expressed in Equation (3) by unit area in a parallel plane. In the above equations, *V* is the volume of the unit cell in a triclinic lattice structure. *a*, *b*, and *c* is the axial lengths and  $\alpha$ ,  $\beta$ , and  $\gamma$  is the axial angles,  $W_{ls}$  is the surface energy of the substrate,  $\sigma_1$  is the surface energy of test liquid, and  $\theta$

is the contact angle. From these calculation, interfacial misfit in <100>, <010>, and <001> direction is 28.3%, 31.0%, and 43.1% respectively. Frank-van der Merwe mode requires a small interfacial misfit of less than a few percent. On the other hand, it is known that the surface energy of Liq is higher than that of the perovskite/PC<sub>70</sub>BM underlayer. The surface energy can be calculated using contact angle experiment, which was referred to by former literature<sup>47,48</sup> and Young-Dupré equation as expressed in Equation (4). The surface energy of Liq and perovskite/PC<sub>70</sub>BM was calculated as 135.7 and 129.5 mJ/m<sup>2</sup>, respectively, so the surface energy difference was 0.046. As a result, the Liq overlayer and perovskite/PC<sub>70</sub>BM underlayer interface exhibits high interfacial misfit and positive surface energy difference that lies on the region of Stranski-Krastanov mode.

The Liq overlayer was deposited onto the perovskite/PC<sub>70</sub>BM underlayer using thermal evaporation. The amount of the deposited Liq was precisely controlled with a thickness monitoring system, and the morphology of the Liq layer with different thicknesses from 0 to 7 nm was observed by the AFM. Figure 3A-C shows the perovskite/PC<sub>70</sub>BM layer without Liq overlayer measured by AFM, friction force microscopy (FFM), C-AFM, respectively. AFM result shown in Figure 3A presents the morphology of the perovskite/PC<sub>70</sub>BM layer by scanning the surface with a sharp tip on a cantilever. The physical scanning process provides the information of frictional force between the tip and the surface caused by molecular adhesion. Figure 3B shows the FFM image of the perovskite/PC<sub>70</sub>BM surface without Liq layer. The friction force mapping on the surface could be determined by various physical and chemical factors such as differences in material, composition, or lattice structure. Figure 3C shows the C-AFM image of the perovskite/PC<sub>70</sub>BM layer. The local current distribution could be measured by mapping the vertical current between the tip and the local area on the surface. Figure 3D-F exhibits the measurement results of 3 nm Liq overlayer onto perovskite/PC<sub>70</sub>BM layer with AFM, FFM, and C-AFM, respectively. The island-like structures of Liq were observed on the surface morphology, as shown in



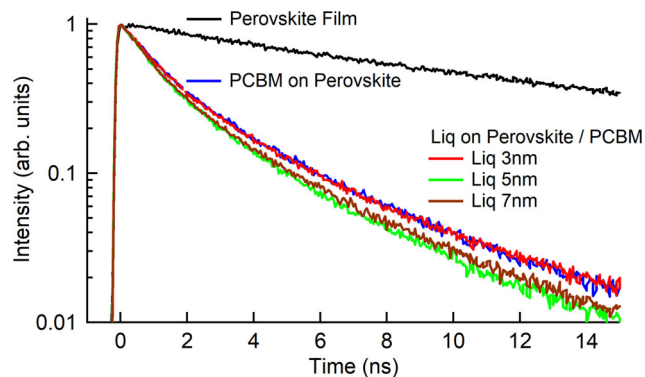
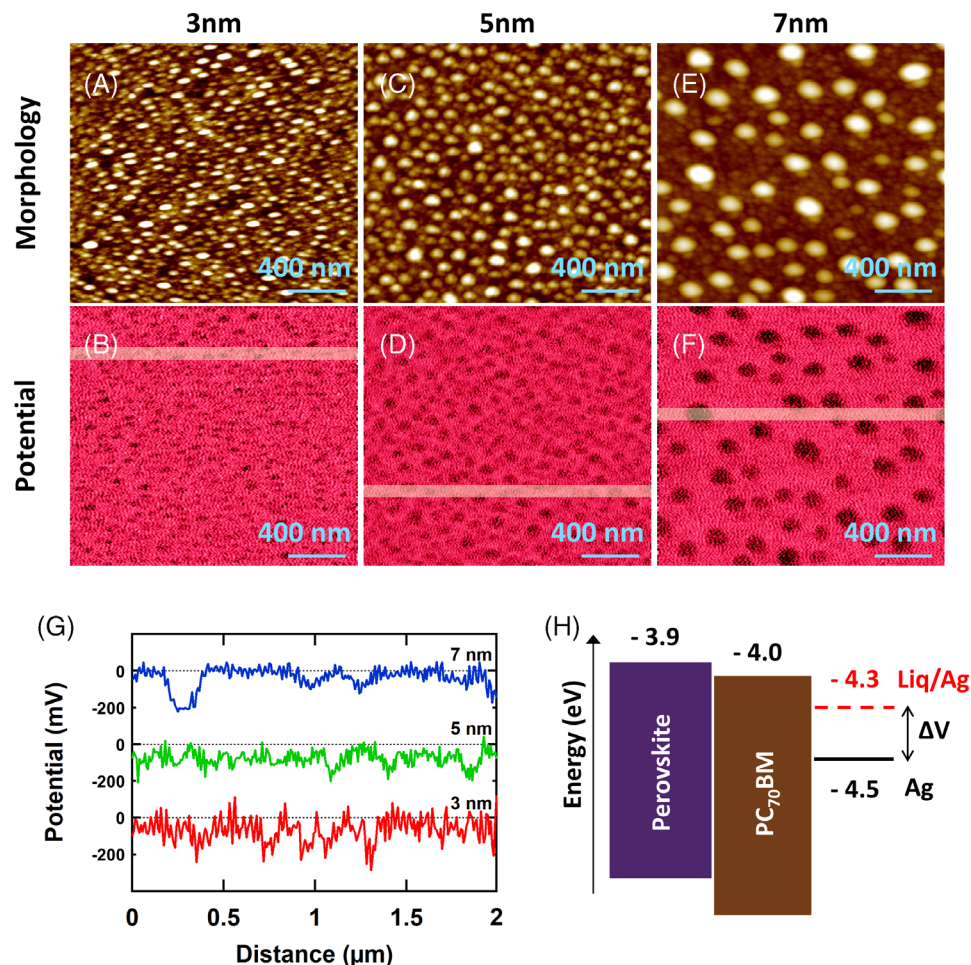
**FIGURE 3** Morphology, lateral force, and conductive morphology of perovskite film with various Liq thickness: A-C, 0 nm; D-F, 3 nm; G-I, 5 nm; J-L, 7 nm. The device structure for C-AFM is ITO/PEDOT:PSS/Perovskite/PC<sub>70</sub>BM/Liq

Figure 3D. FFM result, Figure 3E, supports the formation of island-like Liq film where the friction of the island-like structure is different from the perovskite/PC<sub>70</sub>BM surface. Figure 3G-I shows the measurement results of the 5 nm Liq layer on the perovskite/PC<sub>70</sub>BM layer. At 5 nm of deposition thickness, the Liq layer entirely covered the underneath perovskite/PC<sub>70</sub>BM layer. The island-like structures expanded to the overall surface of the perovskite/PC<sub>70</sub>BM layer, which can be confirmed in Figure 3G. Furthermore, the island-like unique pattern of the friction map for the Liq (3 nm) layer entirely disappeared. The previously listed changes in AFM, C-AFM, and FFM provide that the superlattice of Liq was formed onto the perovskite/PC<sub>70</sub>BM layer. The Liq overlayer and perovskite/PC<sub>70</sub>BM underlayer interface is classified to the Stranski-Krastanov mode with a large interfacial misfit and positive surface energy difference. Therefore, the coverage of Liq film was expanded by increasing the amount of Liq deposition until the superlattice is grown, and it concluded to the superlattice at 5 nm of thickness. Over the larger amount of Liq deposition than the superlattice thickness, the Liq islands were formed again. Figure 3J-L clearly shows the Liq islands were formed again at all AFM, FFM, and C-AFM measurements. As shown in the C-AFM results in Figure 3C,F,I,L, and Figure S9, a relatively higher flow of the vertical current was measured at 3 and 5 nm thickness of Liq. Thus, charge transport through the device was enhanced at the uniform coverage of Liq film. Considering that the AFM cantilever is made of PtIr<sub>5</sub> and behaves like a metal electrode, the uniform coverage of Liq film lowered the charge transport

barrier at the ETL/metal interface, which is speculated to enhance the charge extraction.

To investigate the effect of the Liq layer on the charge transfer barrier, non-contact mode AFM and SKPM were used to analyze the Liq/Ag interface. Figure 4A-F shows the AFM and SKPM images with the different Liq thicknesses of 3, 5, and 7 nm. By increasing Liq thickness, the size of Liq island was increased. While AFM images showed the structure of interfaces between the Liq and Ag layer, SKPM showed the difference of surface potential between the Liq and Ag layer. The surface potential of the Liq deposited area was decreased (colored black) compared to the Ag layer (colored red). The lower surface potential of the Liq/Ag bilayer compared to the Ag monolayer supports the enhanced charge extraction in perovskite solar cells with Liq interlayer. The uniform formation of the Liq interlayer lowered the charge transport barrier from the PC<sub>70</sub>BM layer to the Ag cathode electrode. Figure 4G shows the line profile of surface potential, which was measured by SKPM. The position of the measured profile was highlighted with the white line in Figure 4B,D,F. The surface potential of the Liq/Ag layer exhibited constant value except for the area where Liq island was formed. However, the area of Liq island was measured to have a surface potential of 0.2 eV lower than that of the surrounding area. The correspondence of the surface potential characteristics to the morphology of Liq island formation onto the Ag layer indicated that the Liq/Ag interlayer deposition decreased the surface potential. The amount of surface potential difference was 0.2 eV regardless of the deposition thickness and size of the Liq. Therefore, the prime factor for efficient charge

**FIGURE 4** A–G, AFM, and SKPM measurement of glass/Ag/Liq film with various Liq thickness; H, schematic illustration of energy level shift by Liq insertion



**FIGURE 5** Time-resolved photoluminescence (TR-PL) of the perovskite and perovskite/PC<sub>70</sub>BM bi-layer with various Liq thicknesses

extraction at the Ag electrode would be the fine and uniform coverage of the Liq layer. From Figure 3, the coverage of Liq film was optimized at 5 nm thickness, where the Liq layer forms the superlattice. The performance of perovskite solar cells was also optimized at 5 nm thickness of Liq (Figure 2A).

To further extrapolate the charge extraction property, the time-resolved PL was conducted (Figure 5), and respective parameters were extrapolated (Table 2). As denoted in Equation (5), the curves were fitted by bi-exponential decay. For the pristine perovskite film, the effective PL lifetime (Equation (6)) was 15.221 ns. However, after depositing PC<sub>70</sub>BM on the perovskite film, the effective PL lifetime decreased to 2.321 ns, attributed to the charge extraction property of the PC<sub>70</sub>BM. Furthermore, after depositing Liq on the Perovskite/PC<sub>70</sub>BM, the effective PL lifetime gradually decreased to 1.964 ns, the lowest for the 5 nm of Liq. In line with the *J-V* characteristics (Figure 2) and potential measurements (Figure 4), it is evident that Liq deposition on the perovskite decreases the potential barrier and results in an enhanced charge extraction. However, the effective PL lifetime again increased from 1.964 to 2.035 ns for the 7 nm of Liq. This tendency agrees with various former articles that report the trade-off behavior of the dielectric layers between the energy barrier reduction and charge transfer hindrance, resulting in a drastic drop in device performance for large thickness.<sup>49,50</sup>

	$a_1$	$\tau_1$ (ns)	$a_2$	$\tau_2$ (ns)	$\frac{a_1\tau_1 + a_2\tau_2}{a_1 + a_2}$
Perovskite	0.412	7.207	0.588	20.852	15.221
Perovskite/PC <sub>70</sub> BM	0.693	1.266	0.307	4.702	2.321
Perovskite/PC <sub>70</sub> BM/Liq 3 nm	0.714	1.268	0.286	4.866	2.297
Perovskite/PC <sub>70</sub> BM/Liq 5 nm	0.707	1.118	0.293	4.007	1.964
Perovskite/PC <sub>70</sub> BM/Liq 7 nm	0.708	1.132	0.292	4.226	2.035

TABLE 2 TR-PL coefficient extrapolation and effective PL lifetime

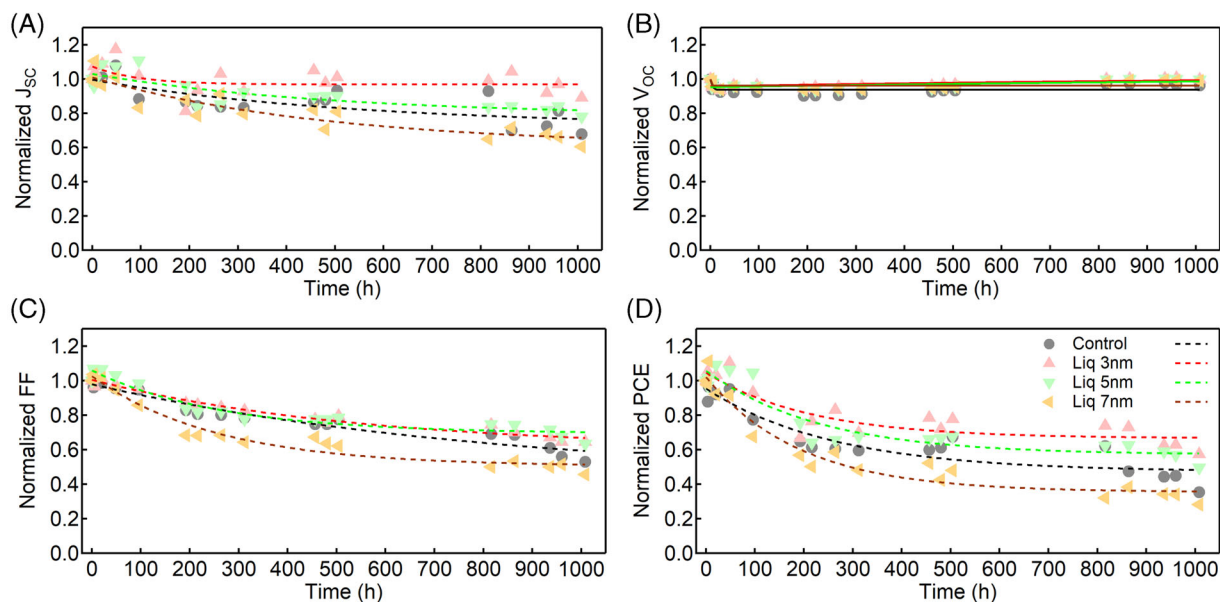


FIGURE 6 Operational stability of A, current density ( $J_{SC}$ ); B, open-circuit voltage ( $V_{OC}$ ); C, fill factor (FF); D, power conversion efficiency (PCE) of PSCs with various Liq thicknesses

$$\frac{I(t)}{I_0} = a_1 e^{-\frac{t}{\tau_1}} + a_2 e^{-\frac{t}{\tau_2}} \quad (5)$$

$$\tau_{eff} = \frac{a_1 \tau_1 + a_2 \tau_2}{a_1 + a_2} \quad (6)$$

### 3.3 | Stability analysis of Liq films on the devices

The operational stability of the PSCs was measured regarding the photovoltaic parameters (Figure 6) under consistent humidity and temperature environments (Figure S10). The degradation points were fitted through the bi-exponential decay, expressed by dashed lines in Figure 6. While the  $V_{OC}$  shows almost no variation during operation regardless of the presence of the Liq layer, the  $J_{SC}$  and FF showed different stability depending on the Liq thickness. The stability of FF improved until the Liq's thickness reached 5 nm, whereas it started to deteriorate when the 7 nm Liq layer was implemented in the

device (Figure 6C). The FF is known to decline when the thickness of the dielectric buffer layer exceeds 5–10 nm.<sup>51</sup> Similarly, the  $J_{SC}$  also showed the highest durability at the Liq's thickness of 3 nm, while at 7 nm, the  $J_{SC}$  showed a smaller value than that of the reference device (Figure 6A). As a result, the combined performance index, PCE, showed the highest stability for the device of Liq's thickness of 3 nm (Figure 6D).

For an in-depth analysis of the decay trends of PSCs with different Liq thicknesses, the iodide migration was analyzed by the TOF-SIMS (Figure 7). Previously, we reported that the iodide migration in the PSCs is vulnerable to the PSCs' operational stability, which tends to accumulate at the interface between the ETL and the cathode.<sup>24</sup> In a fresh device without Liq layer (Figure 7B), the iodide ( $I^-$ ) is gradually detected after the Ag electrode is fully milled without accumulating at the PC<sub>70</sub>BM/Ag interface. However, the aged device showed iodide an ion accumulation peak at the interface (sputter time  $\sim 35$  s) originated from device degradation (Figure 7C). Similarly, the fresh device with Liq (5 nm)

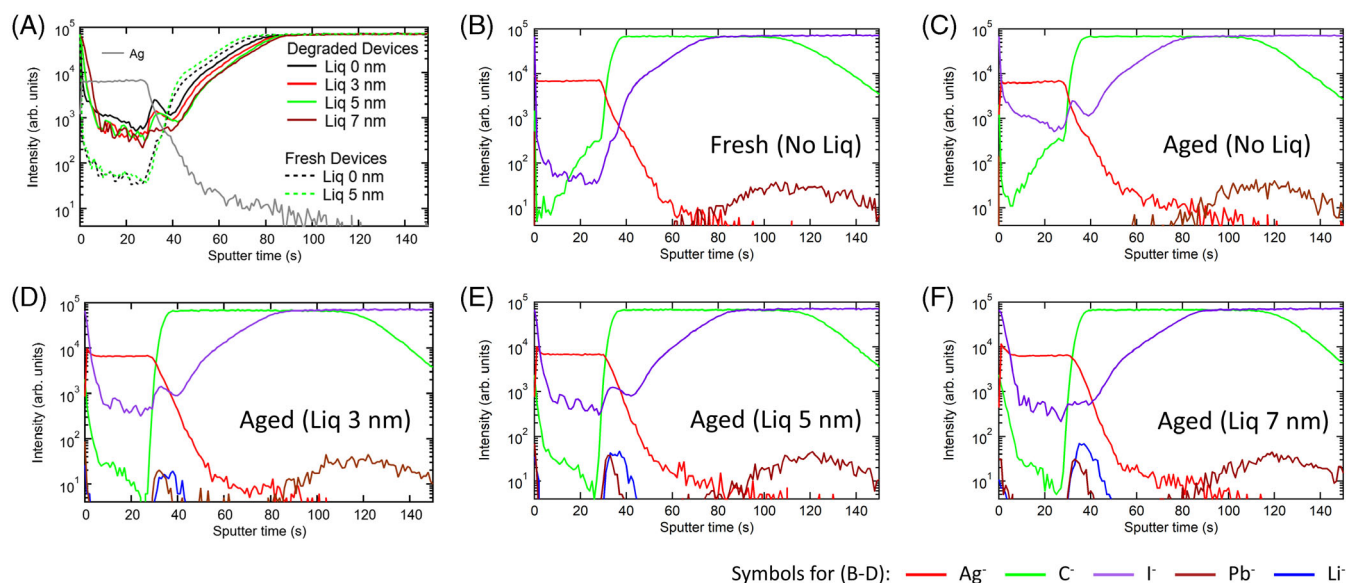


**FIGURE 7** Time-of-flight secondary ion mass spectrometry (TOF-SIMS) of A, iodide signal of the overall devices; B, fresh device without Liq; C, an aged device without Liq; D-F, aged devices with Liq thicknesses of 3, 5, and 7 nm

barely showed iodide accumulation between the ETL and the cathode (Figure 7A). However, iodide accumulation was detected in all aged PSCs, while the magnitude of accumulation varied depending on the Liq thickness. Moreover, iodide ions were migrated into the Ag layer when the devices deteriorated. Along with the increment of Liq thickness, the aged PSCs showed diminished iodide accumulation at the interface. The lowest iodide accumulation could be achieved by implementing a 7 nm Liq layer (Figure 7D-F). Furthermore, the Liq layer is also proved to block the water vapor penetration into the perovskite layer, which prevented the perovskite film degradation with a yellow phase (Figure S11). Thus, we can conclude that the Liq layer effectively inhibits the iodide migration from the perovskite layer to the counter electrode and water vapor penetration from outside during the device operation, which is the fundamental reason for the enhanced stability.

## 4 | CONCLUSIONS

We revealed that the Liq buffer layer in the PSCs acts as an efficient buffer layer, which reduces the potential barrier and elevates the charge extraction. The device with Liq showed increased efficiency from 9.5% to 10.13%, which is mainly originated from the enhanced  $J_{SC}$  and FF. To figure out the reason for the increased charge extraction, surface conductivity and electric potential of Liq-induced devices were measured by C-AFM and SKPM. The insertion of the Liq interlayer reduces the electric barrier between the

PC<sub>70</sub>BM and the Ag electrode. For further insight, the TR-PL measurement was conducted. The insertion of the Liq decreased the effective PL lifetime from 2.321 to 1.964 ns, showing an enhanced charge extraction by the Liq. Besides, PSCs' operational stability concerning the diverse condition was measured. The PSCs with Liq showed significantly improved stability, where the PSC with 3 nm of Liq showed the highest stability. The reason for the stability improvement was revealed through employing the TOF-SIMS analysis. After degradation, while the PSC without Liq showed a severe accumulation of iodide between the PC<sub>70</sub>BM and the Ag electrode, the devices with Liq insertion showed a significantly reduced accumulation between the interface, which is the main reason for the enhanced operation stability. Throughout the overall experiments, we suggested an effective buffer layer candidate for the PSCs, improving both efficiency and operational stability. We believe that our results will provide valuable insights into the PSC fields.

## ACKNOWLEDGEMENTS

This research was supported by the Basic Science Research Program (NRF-2020R1F1A1074263) through the National Research Foundation of Korea (NRF) funded by the Ministry of Education. Hyunho Lee was partially supported in this research by the Basic Science Research Program through the National Research Foundation of Korea (NRF) funded by the Ministry of Education (No. 2018R1A6A1A03025242). The present research has been conducted by the Research Grant of Kwangwoon University in 2020.

## CONFLICT OF INTEREST

The authors declare that they have no known competing financial interests or personal relationships that could have appeared to influence the work reported in this paper.

## ORCID

Kunsik An  <https://orcid.org/0000-0002-4128-0673>

Jaehoon Kim  <https://orcid.org/0000-0002-8723-148X>

Hyunho Lee  <https://orcid.org/0000-0002-7602-1639>

## REFERENCES

- Qin P, Tanaka S, Ito S, et al. Inorganic hole conductor-based lead halide perovskite solar cells with 12.4% conversion efficiency. *Nat Commun*. 2014;5:3834. doi:10.1038/ncomms4834
- Park B-w, Kedem N, Kulbak M, et al. Understanding how excess lead iodide precursor improves halide perovskite solar cell performance. *Nat Commun*. 2018;9:3301. doi:10.1038/s41467-018-05583-w
- Kulkarni SA, Baikie T, Boix PP, Yantara N, Mathews N, Mhaisalkar S. Band-gap tuning of lead halide perovskites using a sequential deposition process. *J Mater Chem A*. 2014;2:9221-9225. doi:10.1039/C4TA00435C
- Rao L, Tang Y, Yan C, et al. Tuning the emission spectrum of highly stable cesium lead halide perovskite nanocrystals through poly(lactic acid)-assisted anion-exchange reactions. *J Mater Chem C*. 2018;6:5375-5383. doi:10.1039/C8TC00582F
- Chen B, Baek S-W, Hou Y, et al. Enhanced optical path and electron diffusion length enable high-efficiency perovskite tandems. *Nat Commun*. 2020;11:1257. doi:10.1038/s41467-020-15077-3
- National Renewable Energy Laboratory. <https://www.nrel.gov/pv/cell-efficiency.html>. (Accessed August 2021).
- Yoon J, Kim U, Yoo Y, et al. Foldable perovskite solar cells using carbon nanotube-embedded ultrathin polyimide conductor. *Adv Sci*. 2021;8:2004092. doi:10.1002/advs.202004092
- Yoon J, Sung H, Lee G, et al. Superflexible, high-efficiency perovskite solar cells utilizing graphene electrodes: towards future foldable power sources. *Energy Environ Sci*. 2017;10:337-345. doi:10.1039/C6EE02650H
- Lee G, Kim M-c, Choi YW, et al. Ultra-flexible perovskite solar cells with crumpling durability: toward a wearable power source. *Energy Environ Sci*. 2019;12:3182-3191. doi:10.1039/C9EE01944H
- Xia F, Wu Q, Zhou P, et al. Efficiency enhancement of inverted structure perovskite solar cells via Oleamide doping of PCBM electron transport layer. *ACS Appl Mater Interfaces*. 2015;7:13659-13665. doi:10.1021/acsami.5b03525
- Zhang M, Chen Q, Xue R, et al. Reconfiguration of interfacial energy band structure for high-performance inverted structure perovskite solar cells. *Nat Commun*. 2019;10:4593. doi:10.1038/s41467-019-12613-8
- Wu C-G, Chiang C-H, Tseng Z-L, Nazeeruddin MK, Hagfeldt A, Grätzel M. High efficiency stable inverted perovskite solar cells without current hysteresis. *Energy Environ Sci*. 2015;8:2725-2733. doi:10.1039/C5EE00645G
- Zhang R, Ling H, Lu X, Xia J. The facile modification of PEDOT:PSS buffer layer by polyethyleneglycol and their effects on inverted perovskite solar cell. *Sol Energy*. 2019;186:398-403. doi:10.1016/j.solener.2019.05.018
- Wang Q, Chueh C-C, Eslamian M, Jen AKY. Modulation of PEDOT:PSS pH for efficient inverted perovskite solar cells with reduced potential loss and enhanced stability. *ACS Appl Mater Interfaces*. 2016;8:32068-32076. doi:10.1021/acsami.6b11757
- Kim Y, Jung EH, Kim G, Kim D, Kim BJ, Seo J. Sequentially fluorinated PTAA polymers for enhancing Voc of high-performance perovskite solar cells. *Adv Energy Mater*. 2018;8:1801668. doi:10.1002/aenm.201801668
- Girolamo DD, Giacomo FD, Matteocci F, et al. Progress, highlights and perspectives on NiO in perovskite photovoltaics. *Chem Sci*. 2020;11:7746-7759. doi:10.1039/D0SC02859B
- Xu L, Chen X, Jin J, et al. Inverted perovskite solar cells employing doped NiO hole transport layers: a review. *Nano Energy*. 2019;63:103860. doi:10.1016/j.nanoen.2019.103860
- Hu C, Bai Y, Xiao S, et al. Surface Sulfuration of NiO boosts the performance of inverted perovskite solar cells. *Sol RRL*. 2020;4:2000270. doi:10.1002/solr.202000270
- Liu D, Wang Q, Traverse CJ, et al. Impact of ultrathin C60 on perovskite photovoltaic devices. *ACS Nano*. 2018;12:876-883. doi:10.1021/acsnano.7b08561
- Lai W-C, Lin K-W, Guo T-F, Chen P, Wang YT. Conversion efficiency improvement of inverted CH<sub>3</sub>NH<sub>3</sub>PbI<sub>3</sub> perovskite solar cells with room temperature sputtered ZnO by adding the C60 interlayer. *Appl Phys Lett*. 2015;107:253301. doi:10.1063/1.4938570
- Yu Z, Yang Z, Ni Z, et al. Simplified interconnection structure based on C60/SnO<sub>2</sub>-x for all-perovskite tandem solar cells. *Nat Energy*. 2020;5:657-665. doi:10.1038/s41560-020-0657-y
- Wang J, Zhang J, Zhou Y, et al. Highly efficient all-inorganic perovskite solar cells with suppressed non-radiative recombination by a Lewis base. *Nat Commun*. 2020;11:177. doi:10.1038/s41467-019-13909-5
- Yu JC, Hong JA, Jung ED, et al. Highly efficient and stable inverted perovskite solar cell employing PEDOT:GO composite layer as a hole transport layer. *Sci Rep*. 2018;8:1070. doi:10.1038/s41598-018-19612-7
- Lee H, Lee C. Analysis of ion-diffusion-induced Interface degradation in inverted perovskite solar cells via restoration of the ag electrode. *Adv Energy Mater*. 2018;8:1702197. doi:10.1002/aenm.201702197
- Yuan Y, Huang J. Ion migration in Organometal Trihalide perovskite and its impact on photovoltaic efficiency and stability. *Acc Chem Res*. 2016;49:286-293. doi:10.1021/acs.accounts.5b00420
- Guo S, Sun X, Ding C, et al. Non-uniform chemical corrosion of metal electrode of p-i-n type of perovskite solar cells caused by the diffusion of CH<sub>3</sub>NH<sub>3</sub>I. *Energy Technol*. 2020;8:2000250. doi:10.1002/ente.202000250
- Zhang Y-N, Li B, Fu L, Li Q, Yin LW. MOF-derived ZnO as electron transport layer for improving light harvesting and electron extraction efficiency in perovskite solar cells. *Electrochim Acta*. 2020;330:135280. doi:10.1016/j.electacta.2019.135280
- Hu W, Yang S, Yang S. Surface modification of TiO<sub>2</sub> for perovskite solar cells. *Trends Chem*. 2020;2:148-162. doi:10.1016/j.trechm.2019.11.002

29. Babaei A, Dreesen C, Sessolo M, Bolink HJ. High voltage vacuum-processed perovskite solar cells with organic semiconducting interlayers. *RSC Adv.* 2020;10:6640-6646. doi: 10.1039/D0RA00214C
30. Fan Y, Fang J, Chang X, et al. Scalable ambient fabrication of high-performance CsPbI<sub>2</sub>Br solar cells. *Joule.* 2019;3:2485-2502. doi:10.1016/j.joule.2019.07.015
31. Tian J, Xue Q, Tang X, et al. Dual interfacial Design for Efficient CsPbI<sub>2</sub>Br perovskite solar cells with improved Photostability. *Adv Mater.* 2019;31:1901152. doi:10.1002/adma.201901152
32. Shao S, Dong J, Duim H, et al. Enhancing the crystallinity and perfecting the orientation of formamidinium tin iodide for highly efficient Sn-based perovskite solar cells. *Nano Energy.* 2019;60:810-816. doi:10.1016/j.nanoen.2019.04.040
33. Sidhik S, Esparza D, Martínez-Benítez A, López-Luke T, Carriles R, de la Rosa E. Improved performance of mesoscopic perovskite solar cell using an accelerated crystalline formation method. *J Power Sources.* 2017;365:169-178. doi:10.1016/j.jpowsour.2017.08.056
34. Kuan C-H, Kuo P-T, Hou C-H, Shyue JJ, Lin CF. Growth process control produces high-crystallinity and complete-reaction perovskite solar cells. *RSC Adv.* 2020;10:35898-35905. doi: 10.1039/D0RA05772J
35. Tailor NK, Abdi-Jalebi M, Gupta V, et al. Recent progress in morphology optimization in perovskite solar cell. *J Mater Chem A.* 2020;8:21356-21386. doi:10.1039/D0TA00143K
36. Chang C-Y, Chu C-Y, Huang Y-C, et al. Tuning perovskite morphology by polymer additive for high efficiency solar cell. *ACS Appl Mater Interfaces.* 2015;7:4955-4961. doi: 10.1021/acsami.5b00052
37. Nukunudompanich M, Budiutama G, Suzuki K, Hasegawa K, Ihara M. Dominant effect of the grain size of the MAPbI<sub>3</sub> perovskite controlled by the surface roughness of TiO<sub>2</sub> on the performance of perovskite solar cells. *CrystEngComm.* 2020;22: 2718-2727. doi:10.1039/D0CE00169D
38. Kyaw AKK, Wang DH, Wynands D, et al. Improved light harvesting and improved efficiency by insertion of an optical spacer (ZnO) in solution-processed small-molecule solar cells. *Nano Lett.* 2013;13:3796-3801. doi:10.1021/nn401267s
39. Lin Y, Shen L, Dai J, et al.  $\pi$ -Conjugated Lewis Base: efficient trap-passivation and charge-extraction for hybrid perovskite solar cells. *Adv Mater.* 2017;29:1604545. doi:10.1002/adma.201604545
40. Zhao X, Tao L, Li H, et al. Efficient planar perovskite solar cells with improved fill factor via Interface engineering with graphene. *Nano Lett.* 2018;18:2442-2449. doi:10.1021/acs.nanolett.8b00025
41. Tsang DP-K, Matsushima T, Adachi C. Operational stability enhancement in organic light-emitting diodes with ultrathin Liq interlayers. *Sci Rep.* 2016;6:22463. doi:10.1038/srep22463
42. Zhang Y, Zu F, Lee S-T, Liao L, Zhao N, Sun B. Heterojunction with organic thin layers on silicon for record efficiency hybrid solar cells. *Adv Energy Mater.* 2014;4:1300923. doi: 10.1002/aenm.201300923
43. Paternò G, Warren AJ, Spencer J, et al. Micro-focused X-ray diffraction characterization of high-quality [6,6]-phenyl-C61-butyric acid methyl ester single crystals without solvent impurities. *J Mater Chem C.* 2013;1:5619-5623. doi: 10.1039/C3TC31075B
44. Begley WJ, Rajeswaran M. Hexakis([mu]-quinolin-8-olato) hexalithium(I): a centrosymmetric doubly stacked trimer. *Acta Crystallogr Sect E.* 2006;62:m1200-m1202. doi:10.1107/S1600536806015601
45. Tu KN. Surface and interfacial energies of CoSi<sub>2</sub> and Si films: implications regarding formation of three-dimensional silicon-silicide structures. *IBM J Res Dev.* 1990;34:868-874. doi: 10.1147/rd.346.0868
46. Saha B, Shakouri A, Sands TD. Rocksalt nitride metal/semiconductor superlattices: a new class of artificially structured materials. *Appl Phys Rev.* 2018;5:021101. doi: 10.1063/1.5011972
47. Kim G-H, Jang H, Yoon YJ, et al. Fluorine functionalized graphene Nano platelets for highly stable inverted perovskite solar cells. *Nano Lett.* 2017;17:6385-6390. doi:10.1021/acs.nanolett.7b03225
48. Chen G, Wang T, Li C, et al. Enhanced photovoltaic performance in inverted polymer solar cells using Li ion doped ZnO cathode buffer layer. *Org Electron.* 2016;36:50-56. doi:10.1016/j.orgel.2016.05.033
49. Wang XJ, Zhao JM, Zhou YC, et al. Enhancement of electron injection in organic light-emitting devices using an ag/LiF cathode. *J Appl Phys.* 2004;95:3828-3830. doi:10.1063/1.1655676
50. Zhao JM, Zhang ST, Wang XJ, et al. Dual role of LiF as a hole-injection buffer in organic light-emitting diodes. *Appl Phys Lett.* 2004;84:2913-2915. doi:10.1063/1.1695444
51. Liu X, Guo LJ, Zheng Y. 5-nm LiF as an efficient cathode buffer layer in polymer solar cells through simply introducing a C60 interlayer. *Nanoscale Res Lett.* 2017;12:543. doi: 10.1186/s11671-017-2299-y

## SUPPORTING INFORMATION

Additional supporting information may be found in the online version of the article at the publisher's website.

**How to cite this article:** An K, Kim J, Yoon B, Lee H. Liq interlayer as electron extraction layer for highly efficient and stable perovskite solar cells. *Int J Energy Res.* 2021;1-11. doi:10.1002/er.7519